

# First-principles calculation of the lattice thermal conductivities of $\alpha$ -, $\beta$ -, and $\gamma$ - $\text{Si}_3\text{N}_4$

Kazuyoshi Tatsumi,<sup>1,2,\*</sup> Atsushi Togo,<sup>2</sup> and Isao Tanaka<sup>2,3,4</sup>

<sup>1</sup>Advanced Measurement Technology Center, Institute of Materials and Systems for Sustainability, Nagoya University, Chikusa, Nagoya 464-8603, Japan

<sup>2</sup>Center for Elements Strategy Initiative for Structural Materials, Kyoto University, Sakyo, Kyoto 606-8501, Japan

<sup>3</sup>Department of Materials Science and Engineering, Kyoto University, Sakyo, Kyoto 606-8501, Japan

<sup>4</sup>Nanostructures Research Laboratory, Japan Fine Ceramics Center, Atsuta, Nagoya 456-8587, Japan

Lattice thermal conductivities of  $\alpha$ -,  $\beta$ - and  $\gamma$ - $\text{Si}_3\text{N}_4$  single crystals are investigated from *ab-initio* anharmonic lattice dynamics, within the single-mode relaxation-time approximation of the linearized phonon Boltzmann transport equation. At 300 K, the lattice thermal conductivity of  $\beta$ - $\text{Si}_3\text{N}_4$  is calculated as  $\kappa_{xx} = 73$  and  $\kappa_{zz} = 198$  (in units of  $\text{Wm}^{-1}\text{K}^{-1}$ ), that is consistent with the reported experimental values of 69 and 180, respectively. For  $\alpha$ - $\text{Si}_3\text{N}_4$ ,  $\kappa_{xx} = 69$  and  $\kappa_{zz} = 99$  are obtained. The difference of anisotropy between  $\alpha$ - $\text{Si}_3\text{N}_4$  and  $\beta$ - $\text{Si}_3\text{N}_4$  is originated from their characteristic difference in the phonon band structures, although their crystal structures are similar in their local atomic coordinates. In  $\alpha$ - $\text{Si}_3\text{N}_4$ , acoustic-mode phonons below 6 THz are the main heat carriers. In  $\beta$ - $\text{Si}_3\text{N}_4$ , the phonon modes up to 12 THz contribute to the lattice thermal conductivity. In  $\gamma$ - $\text{Si}_3\text{N}_4$ ,  $\kappa = 81$  is obtained. The distribution of phonon mode contributions to lattice thermal conductivity with respect to phonon frequency is found to closely resemble  $\kappa_{xx}$  of  $\beta$ - $\text{Si}_3\text{N}_4$  although the phonon lifetimes of  $\gamma$ - $\text{Si}_3\text{N}_4$  are twice shorter than those of  $\beta$ - $\text{Si}_3\text{N}_4$ .

## I. INTRODUCTION

Several nitride insulators are known to exhibit high thermal conductivities and are important for heat transfer materials at elevated temperatures. For example, Slack *et al.*<sup>1</sup> reported that wurtzite-type w-AlN has thermal conductivity of  $\gg 100 \text{ Wm}^{-1}\text{K}^{-1}$ .  $\text{Si}_3\text{N}_4$  has become another promising thermal conductive insulator as its thermal conductivity has been improved up to  $177 \text{ Wm}^{-1}\text{K}^{-1}$  by using the advanced ceramic technologies related to the densification and microstructure control.<sup>2-5</sup> Since the  $\text{Si}_3\text{N}_4$  ceramics also exhibit high mechanical strength at elevated temperatures, they are regarded as ideal materials for the use in various applications, such as engine components, gas turbines, and heat sink substrates of power semiconductor devices.

At atmospheric pressure,  $\text{Si}_3\text{N}_4$  exists in one of two phases,  $\alpha$  and  $\beta$ , which are generally considered as low- and high-temperature phases, respectively.<sup>2,5,6</sup> Their crystal structures belong to the space groups of P31c and P6<sub>3</sub>/m, respectively.<sup>7,8</sup> These structures have different stacking orders of equivalent basal layer structures originated by  $\text{SiN}_4$  tetrahedra.<sup>9</sup> In Fig.1 these layer structures are depicted from the principal direction, as A, B, C, and D in the  $\alpha$  phase and A and B in the  $\beta$  phase. The stacking manners in  $\alpha$ - and  $\beta$ - $\text{Si}_3\text{N}_4$  are thus as ABCDABCD.. and ABAB.., respectively. The  $\alpha$  phase has additional two layer structures of C and D, which are related to the A and B by the *c* glide operation.<sup>9</sup> Along this direction the lattice constant of the  $\alpha$  phase is approximately two times longer than that of the  $\beta$  phase.

The reported values<sup>2-5,11</sup> of the thermal conductivity of the  $\text{Si}_3\text{N}_4$  polymorphs were measured on polycrystalline bulk samples. These values were significantly af-

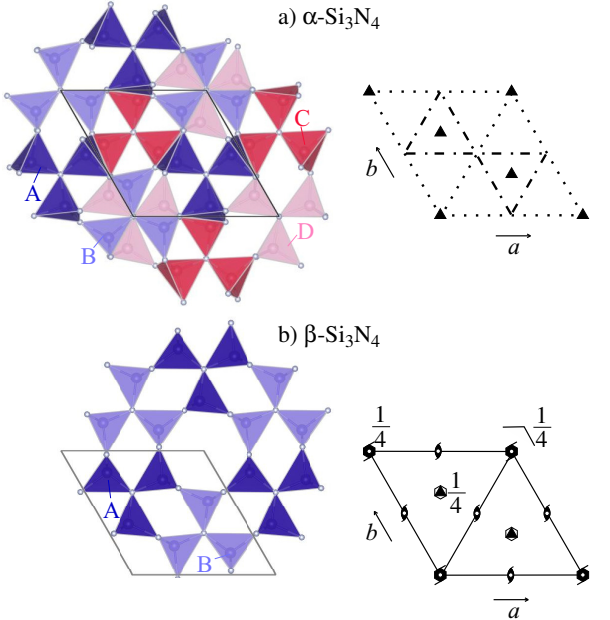


FIG. 1. (color online) Crystal structures of  $\alpha$ - and  $\beta$ - $\text{Si}_3\text{N}_4$ . Stacking of  $\text{SiN}_4$  tetrahedron layers are shown in left. (a) ABCDABCD.. for  $\alpha$ - $\text{Si}_3\text{N}_4$ . (b) ABAB.. for  $\beta$ - $\text{Si}_3\text{N}_4$ . Space group diagrams<sup>10</sup> in P31c ( $\alpha$ - $\text{Si}_3\text{N}_4$ ) and P6<sub>3</sub>/m ( $\beta$ - $\text{Si}_3\text{N}_4$ ) are shown in right.

fected by the contained lattice defects, impurities, shapes and orientations of the constituent crystal grains;<sup>12</sup> the thermal conductivity intrinsic to a defect-free single crystal has not been established. As an experimental access to the intrinsic thermal conductivity, Li *et al.*<sup>13</sup> applied high-resolution thermoreflectance microscopy to a single  $\beta$ - $\text{Si}_3\text{N}_4$  grain in a ceramic sample. The analyzed

thermal conductivities were 69 and 180 Wm<sup>-1</sup>K<sup>-1</sup> along the *a* and *c* axes, respectively. These thermal quantities correspond to the diagonal elements  $\kappa_{xx}$  and  $\kappa_{zz}$  of the lattice thermal conductivity tensor  $\kappa$ . We consider the anisotropy of  $\kappa_{zz}/\kappa_{xx} \sim 3$  is relatively large. Theoretically, Hirosaki *et al.*<sup>12</sup> estimated  $\kappa$  by applying the Green-Kubo formulation to the molecular dynamics (MD) method with the interatomic potentials proposed by Vashishta *et al.*<sup>14</sup>. They calculated  $\kappa_{xx}$  and  $\kappa_{zz}$  of  $\alpha$ -Si<sub>3</sub>N<sub>4</sub> as 105 and 225 Wm<sup>-1</sup>K<sup>-1</sup>, and those of  $\beta$ -Si<sub>3</sub>N<sub>4</sub> as 170 and 450 Wm<sup>-1</sup>K<sup>-1</sup>, respectively. The ratio  $\kappa_{zz}/\kappa_{xx}$  in  $\beta$ -Si<sub>3</sub>N<sub>4</sub> agreed well with the experimental results obtained by Li *et al.*<sup>13</sup>: The  $\kappa_{ii}$  values overestimated the experimental by more than two times.

On many polymorphs of the wurtzite and zincblende structures, the lattice thermal conductivities were recently calculated based on a first principles calculation and Boltzman transport theory.<sup>15</sup> These polymorphs have different stacking orders of the densest atom planes as ABAB.. and ABCABC... The different stacking orders merely altered the lattice thermal conductivities.<sup>15</sup> The phonon linewidth distribution and phonon density of states were similar between the structures as well.<sup>15</sup> On the other hand, the previous MD results on  $\alpha$ - and  $\beta$ -Si<sub>3</sub>N<sub>4</sub> presented that the different stacking orders in these phases altered the  $\kappa$  values largely. The large difference has not been clarified based on the microscopic phonon properties. It is interesting to investigate it using the same approach as in Ref.15 for  $\alpha$ - and  $\beta$ -Si<sub>3</sub>N<sub>4</sub>.

In addition to the  $\alpha$  and  $\beta$  phases, a cubic spinel phase ( $\gamma$ -Si<sub>3</sub>N<sub>4</sub>) is known to form upon compression and in-situ heating.<sup>16,17</sup> The reported transition pressures were scattered from 10 to 36 GPa depending on the experimental conditions.<sup>18</sup> The  $\gamma$  phase is experimentally quenched to atmospheric pressure at room temperature. Its thermal conductivity has not been experimentally reported; it has been estimated only by the Slack model.<sup>19</sup>

The present study aims to qualitatively understand the lattice thermal conductivity tensors among the three Si<sub>3</sub>N<sub>4</sub> phases by means of the first principles approach. We calculate  $\kappa$  of the  $\gamma$  phase as well, for systematic understanding of the lattice thermal conductivity in the Si<sub>3</sub>N<sub>4</sub> system. After the methodology section, we examine the validity of the present results first. Our calculated thermal properties are compared with the available experimental and theoretical references. Then we investigate the characteristics in the calculated  $\kappa$  in detail on the basis of the phonon band structures and phonon linewidths.

## II. COMPUTATIONAL PROCEDURES

### A. Lattice thermal conductivity calculation

The lattice thermal conductivities were calculated by solving the linearized Boltzmann transport equation (LBTE) within the single-mode relaxation time approx-

imation (single-mode RTA). We also tried the direct solution of LBTE<sup>20</sup> and leave its calculated  $\kappa$  values in the following section. The difference in the calculated  $\kappa$  between by the single-mode RTA and by the direct solution was found minor for our discussion. Therefore we limited our research to use the single-mode RTA to take advantage of its intuitive closed form of  $\kappa$ .

In the following sections, we denote a phonon mode by  $\lambda = (\mathbf{q}, p)$  with the set of the phonon wave vector  $\mathbf{q}$  and band index  $p$  and  $-\lambda \equiv (-\mathbf{q}, p)$ . The relaxation time due to phonon-phonon scattering was obtained as reciprocal of linewidth,  $\tau_{\lambda,ph-ph} = (2\Gamma_{\lambda})^{-1}$ , where the linewidth that we employed in this study is as follows:

$$\begin{aligned} \Gamma_{\lambda} = & \frac{18\pi}{\hbar^2} \sum_{\lambda'\lambda''} |\Phi_{-\lambda\lambda'\lambda''}|^2 \times \\ & \{(n_{\lambda'} + n_{\lambda''} + 1)\delta(\omega_{\lambda} - \omega_{\lambda'} - \omega_{\lambda''}) + \\ & (n_{\lambda'} - n_{\lambda''})[\delta(\omega_{\lambda} + \omega_{\lambda'} - \omega_{\lambda''}) - \delta(\omega_{\lambda} - \omega_{\lambda'} + \omega_{\lambda''})]\}. \end{aligned} \quad (1)$$

Here  $\omega_{\lambda}$  is the harmonic phonon frequency of the phonon mode  $\lambda$ ,  $n_{\lambda} = [\exp(\hbar\omega_{\lambda}/k_B T) - 1]^{-1}$  is the Bose-Einstein distribution at temperature  $T$ , and  $\Phi_{\lambda\lambda'\lambda''}$  denotes the three-phonon-scattering strength.  $\Phi_{\lambda\lambda'\lambda''}$  was obtained by usual coordinate transformation of third-order force constants from direct space to phonon space.<sup>15</sup> The second- and third-order real-space force constants were obtained from the *ab-initio* calculation, whose details are written in the next section.

In order to compare the more realistic results of the calculated  $\kappa$  with the experimental data, the isotopic scattering effect due to the natural isotope distribution was taken into account according to the second-order perturbation theory.<sup>21</sup> With the relaxation times of the phonon-phonon scattering and isotopic scattering,  $\tau_{\lambda,ph-ph}$  and  $\tau_{\lambda,iso}$ , the total relaxation time for a phonon mode was assumed to be  $1/\tau_{\lambda} = 1/\tau_{\lambda,ph-ph} + 1/\tau_{\lambda,iso}$ , according to Matthiessen's rule.

The available experimental thermal conductivity data of the Si<sub>3</sub>N<sub>4</sub> system have been measured on the polycrystalline samples and not measured from any single crystals. In order to consider the effect of various lattice defects in the polycrystalline samples, such as grain boundaries, impurities, and vacancies, we crudely took them into account by a relaxation time  $\tau_{\lambda,bs} = L/|\mathbf{v}_{\lambda}|$  of a phonon boundary scattering model, where  $\mathbf{v}_{\lambda} = \nabla_{\mathbf{q}}\omega_{\lambda}$  is the group velocity and  $L$  a parameter regarding to the boundary mean free path. We consider  $\tau_{\lambda,bs}$  as a variable parameter and included it to  $\kappa$  according to Matthiessen's rule.

The closed form of  $\kappa$  within RTA was obtained via

$$\kappa(T) = \frac{1}{N_{\mathbf{q}}\Omega} \sum_{\lambda} \tau_{\lambda}(T) \mathbf{v}_{\lambda} \otimes \mathbf{v}_{\lambda} c_{\lambda}(T), \quad (2)$$

where  $N_{\mathbf{q}}$  is the number of  $\mathbf{q}$ -points,  $\Omega$  is the unit cell volume, and  $c_{\lambda}$  is the mode heat capacity. To analyze  $\kappa$  in

detail, we calculate the cumulative thermal conductivity:

$$\kappa^c(\omega) = \frac{1}{N_q\Omega} \int_0^\omega \sum_\lambda \tau_\lambda(T) \mathbf{v}_\lambda \otimes \mathbf{v}_\lambda c_\lambda(T) \delta(\omega' - \omega) d\omega', \quad (3)$$

and its derivative  $\frac{\partial \kappa^c(\omega)}{\partial \omega}$  to see the phonon mode contributions to  $\kappa$ .

The lattice thermal conductivities were calculated with the phonon-phonon interaction calculation code PHONO3PY<sup>15</sup>, while the harmonic phonon states were analyzed with the phonon calculation code PHONOPY<sup>22</sup>.

## B. Computational details

The force constants were calculated using the first-principles projector augmented wave method<sup>23</sup> (VASP code<sup>24–26</sup>). The generalized gradient approximation (GGA) parameterized by Perdew, Burke, and Ernzerhof<sup>27</sup> was used for the exchange correlation potential. A plane wave energy cutoff of 500 eV was employed. The crystal structures were optimized until the residual forces acting on the constituent atoms was less than  $10^{-6}$  eV/Å. The structural optimization was firstly performed for a temperature of 0 K and 0 GPa. Here the temperature and pressure were considered only for the electronic system and the zero point lattice vibration was not taken into account. The calculated lattice parameters were  $a = 7.808$  Å and  $c = 5.659$  Å for the  $\alpha$  phase,  $a = 7.660$  Å and  $c = 2.925$  Å for the  $\beta$  phase, and  $a = 7.787$  Å for the  $\gamma$  phase, which agree with the experimental data<sup>7,8,28</sup> within +0.7 % errors. The lattice volume optimized within the local density approximation (LDA)<sup>29</sup> for the exchange correlation potential was, for  $\beta\text{-Si}_3\text{N}_4$ , 3 % smaller than within GGA, which is a typical volume contraction of LDA. The  $\kappa$  calculated within LDA was larger by 2.6 % than within GGA. For our discussion, this difference is enough small, therefore the impact of choice of exchange correlation potential is considered to be minor in our study.

Supercell and finite difference approaches were used to calculate the force constants.<sup>30</sup> The supercells were  $1 \times 1 \times 2$ ,  $1 \times 1 \times 3$ , and  $1 \times 1 \times 1$  supercells of the conventional unit cells for the calculation of the third-order force constants in  $\alpha$ ,  $\beta$ , and  $\gamma\text{-Si}_3\text{N}_4$ , respectively; they were  $3 \times 3 \times 4$ ,  $3 \times 3 \times 8$  and  $2 \times 2 \times 2$  for the second-order force constants. The length of the induced atomic displacement was set to 0.03 Å. Table I shows the  $\kappa$  calculated with several different sets of the supercells, indicating that our calculated  $\kappa$  is reasonably converging with respect to the size of the supercells.

Non-analytical term correction<sup>31</sup> was applied to the second-order force constants to take into account the long range Coulomb forces present in ionic crystals. For the correction, Born effective charges were calculated by using the density functional perturbation theory

TABLE I. Calculated lattice thermal conductivities of  $\alpha$ -,  $\beta$ -, and  $\gamma\text{-Si}_3\text{N}_4$  ( $\text{WK}^{-1}\text{m}^{-1}$ ) at 300 K with respect to several combinations of supercell sizes.

Phase	Supercell (# of atoms)		LTC	
	3 <sup>rd</sup> force constants	2 <sup>nd</sup> force constants	<i>xx</i>	<i>zz</i>
$\alpha$	1 $\times$ 1 $\times$ 1 (28)	1 $\times$ 1 $\times$ 1 (28)	37	57
	1 $\times$ 1 $\times$ 2 (56)	1 $\times$ 1 $\times$ 2 (56)	41	79
	1 $\times$ 1 $\times$ 1 (28)	2 $\times$ 2 $\times$ 2 (224)	55	81
	1 $\times$ 1 $\times$ 2 (56)	2 $\times$ 2 $\times$ 2 (224)	67	95
	1 $\times$ 1 $\times$ 2 (56)	2 $\times$ 2 $\times$ 3 (336)	68	97
	1 $\times$ 1 $\times$ 2 (56)	3 $\times$ 3 $\times$ 4 (1008)	68	100
$\beta$	1 $\times$ 1 $\times$ 2 (28)	1 $\times$ 1 $\times$ 2 (28)	44	173
	1 $\times$ 1 $\times$ 2 (28)	2 $\times$ 2 $\times$ 4 (224)	76	208
	1 $\times$ 1 $\times$ 3 (42)	2 $\times$ 2 $\times$ 4 (224)	71	194
	1 $\times$ 1 $\times$ 3 (42)	2 $\times$ 2 $\times$ 5 (280)	72	196
	1 $\times$ 1 $\times$ 3 (42)	3 $\times$ 3 $\times$ 8 (1008)	73	199
$\gamma$	1 $\times$ 1 $\times$ 1 (56)	1 $\times$ 1 $\times$ 1 (56)	72	
	1 $\times$ 1 $\times$ 1 (56)	2 $\times$ 2 $\times$ 2 (448)	77	
	1 $\times$ 1 $\times$ 1 (56)	3 $\times$ 3 $\times$ 3 (56)	79	

## (DFPT).Ref!

Uniform  $\mathbf{k}$ -point sampling meshes of  $4 \times 4 \times 2$ ,  $4 \times 4 \times 3$ , and  $3 \times 3 \times 3$  were used for the third-order force constants of the  $\alpha$ ,  $\beta$ , and  $\gamma$  phases. For the  $\alpha$  and  $\beta$  phases the center of the  $a^* \text{-} b^*$  plane was sampled while the center on the  $c^*$ -axis was not. For the  $\gamma$  phase, non- $\Gamma$  center mesh was used. For the second-order force constants, the  $\Gamma$ -point was only sampled for the  $\alpha$  and  $\beta$  phase and the only one  $\mathbf{k} = (0.5, 0.5, 0.5)$  point was sampled for the  $\gamma$  phase. The  $\mathbf{q}$ -point sampling meshes of  $10 \times 10 \times 14$ ,  $10 \times 10 \times 26$ , and  $12 \times 12 \times 12$  were used to calculate  $\kappa$  in Eq. (2) for the  $\alpha$ ,  $\beta$ , and  $\gamma$  phases.

We examined the effect of thermal expansion on  $\kappa$  by calculating them with the crystal structures optimized for several finite temperatures within the quasi-harmonic approximation (QHA)<sup>32</sup>. The structure was optimized for a temperature and 0 GPa so as to show a minimum Helmholtz free energy.  $\kappa$  for the temperature was calculated with the optimized structure. This  $\kappa$  was differed from the one for the temperature, calculated with the structure optimized for 0 K and 0 GPa. We consider that this difference is caused by the thermal expansion of the lattice. For  $\beta\text{-Si}_3\text{N}_4$  and the temperatures of 300, 600, 900, 1200, and 1500 K, the differences in  $\kappa$  between the two structures were found less than 1 %, similar to the case of Si and Ge<sup>33</sup>. For the present study, these differences are negligible and we adopt the  $\kappa$  calculated with the structure optimized for 0 K and 0 GPa.

We calculated the volumetric thermal expansion coefficients and compared them with the reported experimental values so as to check the validity of the present thermal conductivity calculation, because the thermal expansion is originated from the anharmonicity of the interatomic potential as well as  $\kappa$ . The calculated val-

ues of the  $\alpha$  and  $\beta$  phases are  $4.31 \times 10^{-6}$  and  $4.19 \times 10^{-6} \text{ K}^{-1}$  for 300 K, while the experimental values<sup>34</sup> were  $3.75 \times 10^{-6}$  and  $3.55 \times 10^{-6} \text{ K}^{-1}$ . The present calculation reproduced the experimental tendency where the  $\alpha$  phase has a slightly larger thermal expansion coefficient than the  $\beta$  phase, supporting that the present calculations enable us to qualitatively compare the calculated  $\kappa$  of the  $\text{Si}_3\text{N}_4$  phases.

In order to compare the microscopic phonon properties among the three phases at the same conditions, those results calculated at 0 GPa are shown and discussed. For the  $\gamma$  phase, this means that we assume the condition of a virtually quenched  $\gamma$  phase at 0 GPa from the high pressure. To examine the analytical continuity of the properties with respect to pressures, we calculated  $\kappa$  of the  $\gamma$  phase at 10, 20, and 40 GPa as shown in Fig. 8. The phenomenological behaviour of linear dependence of  $\kappa$  with respect to pressure was reproduced as similar to Ref. 35. The slope was  $2.89 \text{ Wm}^{-1}\text{K}^{-1}\text{GPa}^{-1}$  for the  $\gamma$  phase. By this dependence, we consider that the microscopic values are also varied smoothly with the pressure and those at 0 GPa are valuable to compare with the  $\alpha$  and  $\beta$  phases.

### C. Direct solution of LBTE

The merit to employ the single-mode RTA for thermal conductivity calculation is the closed form, by which we can intuitively understand the qualitative character of  $\kappa$  in terms of the relaxation time and group velocity. The microscopic understanding of the full solution of LBTE is still under the development<sup>36</sup> and the microscopic picture based on collective phonons<sup>37</sup> will require more complicated investigation although it is known that the single-mode RTA solution of LBTE often underestimates the full solution.<sup>33,38</sup>

On the  $\kappa$  of the  $\alpha$  and  $\beta$  phases, we adopted a direct solution of LBTE<sup>20</sup>, which is one of the methods of LBTE full solutions. Their  $\kappa_{xx}$  and  $\kappa_{zz}$  without the isotope effect were 69 and  $102 \text{ Wm}^{-1}\text{K}^{-1}$  for the  $\alpha$  phase and 76 and  $238 \text{ Wm}^{-1}\text{K}^{-1}$  for the  $\beta$  phase, respectively, while the corresponding single-mode RTA values were 70 and  $102 \text{ Wm}^{-1}\text{K}^{-1}$  for the  $\alpha$  phase and 76 and  $210 \text{ Wm}^{-1}\text{K}^{-1}$  for the  $\beta$  phase. The  $\kappa_{zz}$  of the direct solution in the  $\beta$  phase was 13 % larger than that of the single-mode RTA solution. Since the differences in  $\kappa$  between the LBTE solutions are not significant, we expect the physics on those lattice thermal conductivities is well understood within RTA in the current level of our interest. **Therefore, we discuss the lattice thermal conductivities using the results of the single-mode RTA solution.**

TABLE II. Calculated thermal conductivities of  $\alpha\text{-Si}_3\text{N}_4$  (trigonal),  $\beta\text{-Si}_3\text{N}_4$  (trigonal), and  $\gamma\text{-Si}_3\text{N}_4$  (cubic) at 300 K, compared with the experimental data. Theoretical bulk moduli  $B$  in units of GPa, calculated by the authors by using the present band method, are presented in the fourth column.

	This work		$\kappa$	Ref. Theo.		Ref. Expt.	
	$\kappa_{xx}$	$\kappa_{zz}$		$\kappa_{xx}$	$\kappa_{zz}$	$\kappa_{xx}$	$\kappa_{zz}$
$\alpha\text{-Si}_3\text{N}_4$	68	100	224	70 <sup>a</sup>	105 <sup>b</sup>	225 <sup>b</sup>	-
$\beta\text{-Si}_3\text{N}_4$	73	199	237	250 <sup>a</sup>	170 <sup>b</sup>	450 <sup>b</sup>	69 <sup>c</sup> 180 <sup>c</sup>
$\gamma\text{-Si}_3\text{N}_4$	77	-	296	80 <sup>a</sup>	-	-	-

<sup>a</sup> Ref. 19, Slack model.

<sup>b</sup> Ref. 12, molecular dynamics (Green-Kubo).

<sup>c</sup> Ref. 13, single crystalline grains of poly-crystals.

## III. RESULTS AND DISCUSSION

### A. Lattice thermal conductivities

Table II shows the present results of the  $\kappa$  for 300 K.  $\beta\text{-Si}_3\text{N}_4$  has markedly more anisotropic  $\kappa$  than  $\alpha\text{-Si}_3\text{N}_4$ . The directional averages  $\sum_i \kappa_{ii}/3$  are 79, 115, and 77  $\text{Wm}^{-1}\text{K}^{-1}$  for the  $\alpha$ ,  $\beta$ , and  $\gamma$  phases, respectively. The value of the  $\gamma$  phase is similar to that of the  $\alpha$  phase, in spite of comparatively large difference among the bulk moduli ( $B$ ) that are also shown in Table II.

Table II also shows the previously reported experimental<sup>13</sup> and theoretical<sup>12</sup> thermal conductivities for the references. Previously Morelli *et al.*<sup>19</sup> employed the Slack model for estimating the lattice thermal conductivities of the three phases. They are shown as  $\kappa$  in Table II. For the  $\beta$  phase, our  $\kappa$  agrees better with the experimental, than that of the molecular calculation<sup>12</sup> does. Also, our directional average  $\sum_i \kappa_{ii}/3$  ( $115 \text{ Wm}^{-1}\text{K}^{-1}$ ) agrees better with the experimental average ( $106 \text{ Wm}^{-1}\text{K}^{-1}$ ), than the Slack model does.

Fig. 2 shows the theoretical  $\kappa$  of the  $\alpha$  and  $\beta$  phases as a function of  $T$ , together with the reference experimental data<sup>5,11,13</sup>. The thermal conductivities for a series of temperatures were only reported on the polycrystalline bulk samples. These bulk thermal conductivities cannot be directly compared with the calculated intrinsic  $\kappa$  because the microstructures of the bulk samples largely affected the bulk thermal conductivities: They were deviated from the simple directional averages of the intrinsic  $\kappa_{ii}$ , depending on the shapes of the constituent crystal grains. We treated this effect by using a parameter  $0 \leq w \leq 1$  and fitting quantities of  $w\kappa_{xx} + (1-w)\kappa_{zz}$  to the experimental bulk thermal conductivities by the least squares method. We consider these as theoretical bulk thermal conductivities

In Fig. 2, the  $\kappa_{ii}$  calculated without  $\tau_{\lambda,\text{bs}}$  are nearly proportional to  $T^{-1}$  because  $n_\lambda$  in Eq. (1) can be reduced to  $\exp(-\hbar\omega_\lambda/k_B T)$ . In Fig. 2-a, the temperature dependence of the experimental bulk thermal conductivities of a chemically vapor-deposited  $\alpha\text{-Si}_3\text{N}_4$  sample<sup>11</sup> is

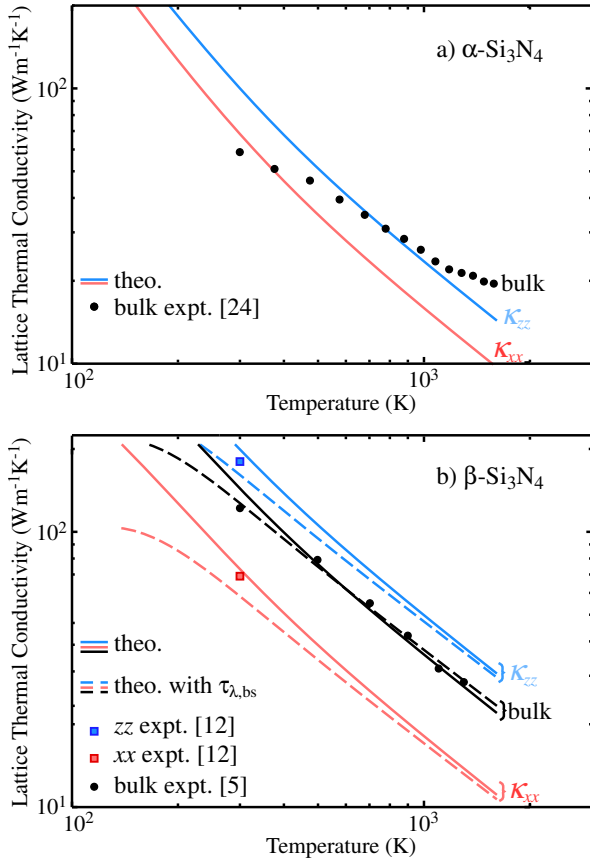


FIG. 2. (color online) Temperature dependence of thermal conductivities for  $\alpha$ - and  $\beta$ - $\text{Si}_3\text{N}_4$ . For  $\beta$ - $\text{Si}_3\text{N}_4$ , theoretical results with the boundary scattering effect are shown by broken lines. Theoretical bulk thermal conductivities (see in text) for the  $\beta$ - $\text{Si}_3\text{N}_4$  sample are also shown to be compared with the experimental bulk thermal conductivities.

deviated from inverse proportion considerably, intersecting the theoretical lines. Thus no value of  $w$  adjusts the theoretical conductivities to the experimental data. The full solution of LBTE would negligibly cure the disagreement. Including the simple phonon lifetime of boundary scattering,  $\tau_{\lambda,\text{bs}} = L/|\mathbf{v}_{\lambda}|$ , into the total phonon lifetime according to Matthiessen's rule, could not explain the discrepancy as well. A  $L$  value of  $0.6 \mu\text{m}$ , which was much smaller than the experimental grain size<sup>11</sup> of  $10 \mu\text{m}$ , decreased the room-temperature theoretical  $\kappa_{xx}$  and  $\kappa_{zz}$  values toward the experimental values, but severely underestimated the experimental values in the high temperature side. At present, the reason for the discrepancy between the theoretical and experimental behaviors is unclear. Although the crystal structure of the experimental sample was characterized as  $\alpha$ - $\text{Si}_3\text{N}_4$ , significant lattice defects might exist in the as-deposited sample as pointed out by Hirosaki *et al.*<sup>12</sup> and the simple phonon boundary scattering model might fail to describe their effects on the bulk thermal conductivities.

The experimental bulk thermal conductivities of the  $\beta$

phase are located in-between the theoretical  $\kappa_{xx}$  and  $\kappa_{zz}$ , being nearly proportional to  $T^{-1}$ . Simple directional averages of the theoretical  $\kappa_{ii}$  slightly underestimate these experimental values. This is understood from the fact that the microstructure was controlled to improve the thermal conductivity, and the crystalline grains were selectively grown along the  $c$  axis of the most conductive direction.<sup>5</sup> The theoretical bulk thermal conductivities were fit well with  $w = 0.44$  to the experimental bulk thermal conductivities. For the effects of lattice defects most of which were grain boundaries, we included  $\tau_{\lambda,\text{bs}}$  with  $L = 0.6 \mu\text{m}$  to further fit the theoretical curve ( $w = 0.33$ ) to the experimental data. The  $L$  value is slightly smaller than the average grain size<sup>5</sup> ( $2 \mu\text{m}$ ) of the experiment. The experimental  $\kappa_{ii}$  are rather close to the theoretical  $\kappa_{ii}$  calculated without  $\tau_{\lambda,\text{bs}}$ . This is explained by the fact that the experimental  $\kappa_{xx}$  and  $\kappa_{zz}$  were deduced consistently through the grains of several different sizes. The effects of the phonon scattering at the grain boundaries were eliminated.<sup>13</sup>

## B. Dispersion curves

Figure 3 shows the phonon band diagrams of the three  $\text{Si}_3\text{N}_4$  phases. The entire band diagrams are almost identical to those reported earlier<sup>18,39</sup>. However, here we investigate the group velocities projected on the high-symmetry paths, especially focusing on their anisotropy of the  $\alpha$  and  $\beta$  phases. This was not investigated by the previous works.

The  $\omega_{\lambda}$  on the acoustic branches in the  $\beta$  phase increase much more from  $\Gamma$  to  $A$  than from  $\Gamma$  to  $K$  or  $M$ . In the  $\alpha$  phase, the corresponding  $\omega_{\lambda}$  increase more equally among the paths. This difference is due to the different  $\Gamma$ - $A$  path lengths. The  $\beta$  phase has an approximately twice longer path than the  $\alpha$  phase; the lattice constant  $c$  of the  $\beta$  phase is nearly half that of the  $\alpha$  phase, owing to the difference in the stacking manner of the basal layers. Normally, optical branches are flat; however, the upper branches along the  $\Gamma$ - $A$  path also have significantly large gradients in the  $\beta$  phase. These findings indicate that the  $\beta$  phase contains a larger number of phonon modes whose  $v_{\lambda,z}$  is large and whose  $\mathbf{v}_{\lambda}$  orients to the  $c$  axis direction. We will show this tendency further in the following sections.

In the  $\gamma$  phase, the acoustic phonon branches show significant linear dispersions on the  $\Gamma$ - $L$  and  $\Gamma$ - $X$  paths. The roughly constant gradients of  $\omega_{\lambda}$  are large, reflecting the large elastic constants of the  $\gamma$  phase as shown in Table II.

## C. $\omega_{\lambda}$ counter map on reciprocal plane

We show the anisotropy in the group velocities on another geometry, that is, a cross-section of the Brillouin-zone. In Fig. 4, we show the distributions on the  $b^*$ - $c^*$



FIG. 3. (color online) Brillouin-zones (left) and calculated phonon band diagrams (right) for three  $\text{Si}_3\text{N}_4$  phases.

plane. The distributions for four bands from the lowest frequency are shown, because these bands contribute significantly to the  $\kappa$ . We did not find any significant differences in the distributions between the  $b^*-c^*$  plane and the other planes containing the  $c^*$  axis. Thus we select the  $b^*-c^*$  plane as a representative plane. In the  $\alpha$  phase, the distributions are nearly isotropic. Their gradients, the group velocities projected onto the  $b^*-c^*$  plane, are thus nearly isotropic. On the other hand, in the  $\beta$  phase, the iso-frequency lines in  $0.06 \leq q_{c^*} \leq 0.12 \text{ \AA}^{-1}$  are rather parallel to the  $q_{b^*}$  axis, confirming that the four bands of the  $\beta$  phase, in a significantly large part of the Brillouin zone, have  $\mathbf{v}_\lambda$  oriented to the  $c$  axis direction.

#### D. Frequency-dependences of $\kappa^c$ , $\mathbf{v}_\lambda$ and $\Gamma_\lambda$

We have investigated in the previous two sections the anisotropy in the  $\mathbf{v}_\lambda$  for obtaining an insight on the anisotropy in the  $\kappa$ . Here we completely investigate the characteristic points in the  $\kappa$  by using the important phonon properties existing in the closed form of RTA

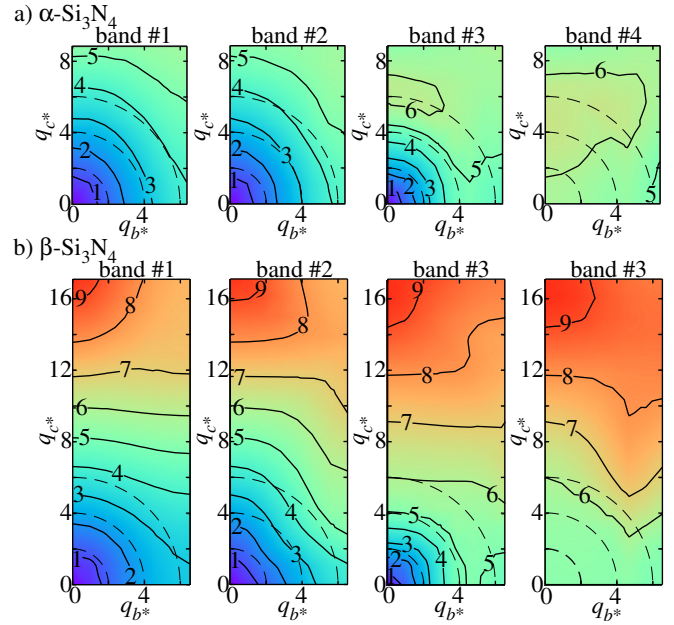


FIG. 4. (color online) Contour maps of phonon frequency (THz) on the  $b^*-c^*$  planes of Brillouin-zones. The coordination in the reciprocal plane are in units of  $10^{-2} \text{ \AA}^{-1}$ . The maps for the four lowest-frequency phonon states are shown. The frequency landscapes are formed by simply connecting the frequencies of the same band indices, assigned by ascending order of frequency at the respective  $\mathbf{q}$  points.

in Eq. (2). These properties are taken over the Brillouin zone because the  $\kappa$  is a quantity integrated there. In order to visually show the similarity or difference in these properties among the phases, we plot in Fig. 5 their frequency distributions: The phonon density of states (DOS) shows the distribution of the heat carriers. The cumulative thermal conductivities  $\kappa^c$  show the phonon frequencies where the phonons largely contribute to the  $\kappa$ . Their first derivatives are also shown to clearly identify these frequencies. By weighting the DOS with  $v_{\lambda,i}^2$ , we show the impacts of the  $v_{\lambda,i}$  and carrier density together. We abbreviate these weighted DOS as WDOS. The phonon linewidth is the remaining important property. To avoid from double counting of the carrier density, scatter plots of  $(\Gamma_\lambda, \omega_\lambda)$  are employed to compare their impacts.

The distinct first peaks in the DOS are indicated by arrows in Fig. 5-a. They are roughly related to the flattening of the acoustic branches near the Brillouin zone boundaries. It is interesting that only  $\kappa^c$  in the  $\beta$  phase increase significantly in the higher frequency range beyond the peak. This is due to the anisotropic dispersions of the acoustic phonon branches and the large gradients of the low frequency optical phonon branches.

Compared the four kinds of phonon properties among the three phases, the DOS, WDOS and  $\Gamma_\lambda$  distribution of the  $\gamma$  phase are much different from the other phases. These large differences are consistent with the large dif-

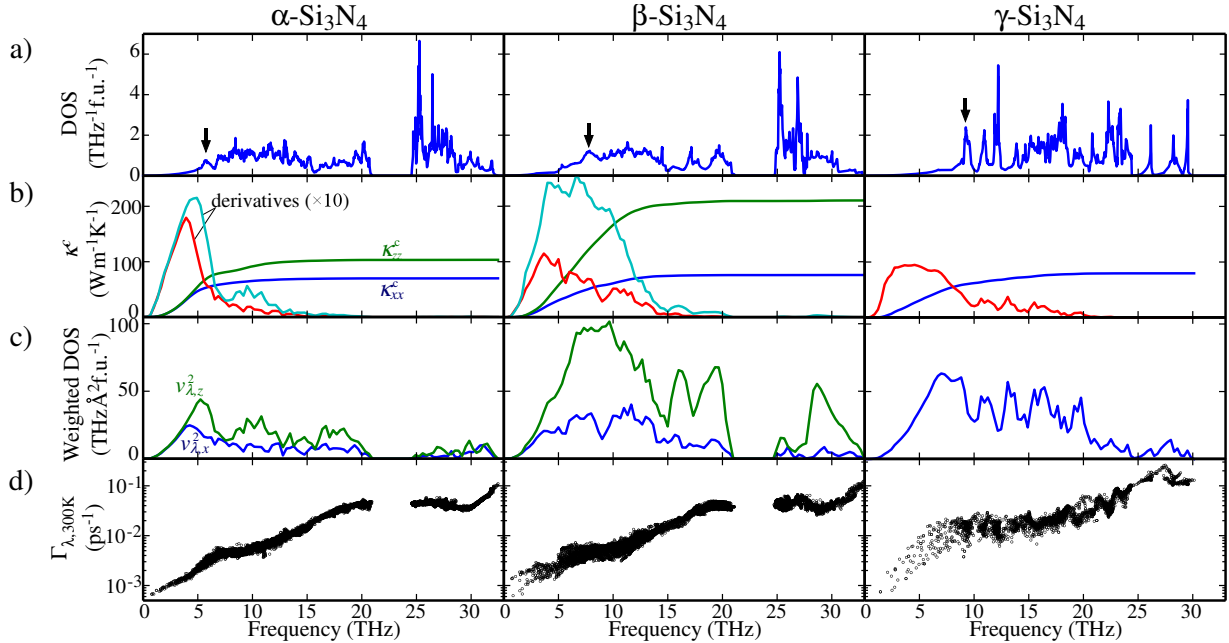


FIG. 5. (color online) Microscopic phonon properties of three  $\text{Si}_3\text{N}_4$  phases. Cumulative thermal conductivity  $\kappa^c$  and its derivative (a), DOS (b), weighted DOS with  $v_{\lambda,i}^2$  (c) and linewidth  $\Gamma_\lambda$  (d).

ferences in the crystal structure. Some characteristic points are explained by the chemical bonding of the  $\gamma$  phase. (1) In the DOS, the first peak is located at a higher frequency than the other phases. This is consistent with the finding in the band diagram; the linear dispersions of the acoustic phonon branches with the large gradients, reflecting the strong chemical bonding consistent with the large bulk modulus. (2) The WDOS is larger than the other phases in the most part of the frequency range where  $\frac{d\kappa_{ii}^c}{d\omega_\lambda}$  is large. This is also explained by the large gradients of the dispersions. (3) The linewidths are also larger than the other phases in the frequency range. For this, the three-phonon-scattering strength  $\Phi_{\lambda\lambda'\lambda''}$  is shortly investigated here. In Table. III, the magnitudes of  $\Phi_{-\lambda\lambda'\lambda''}$  are compared as the averages over two frequency ranges of  $\omega_\lambda$  and all  $(\lambda', \lambda'')$ . The values between 0–15 THz of the  $\gamma$  phase are much larger than the other phases. This is consistent with the larger linewidths. As a result of the *opposite* impacts of the linewidth and WDOS, the  $\kappa_{xx}^c$  resembles closely to  $\kappa_{xx}^c$  of the  $\beta$  phase.

TABLE III. Averages of  $\Phi_{-\lambda\lambda'\lambda''}$  over frequency ranges of  $\omega_\lambda$  (0–15 and 0–35 THz) and all  $(\lambda', \lambda'')$ . The values are in units of  $10^{-10} \text{ eV}^2 \text{f.u.}^{-1}$ .

Frequency Range (THz)	Phase		
	$\alpha$	$\beta$	$\gamma$
0–15	2.66	2.63	5.76
0–30	13.1	13.0	11.4

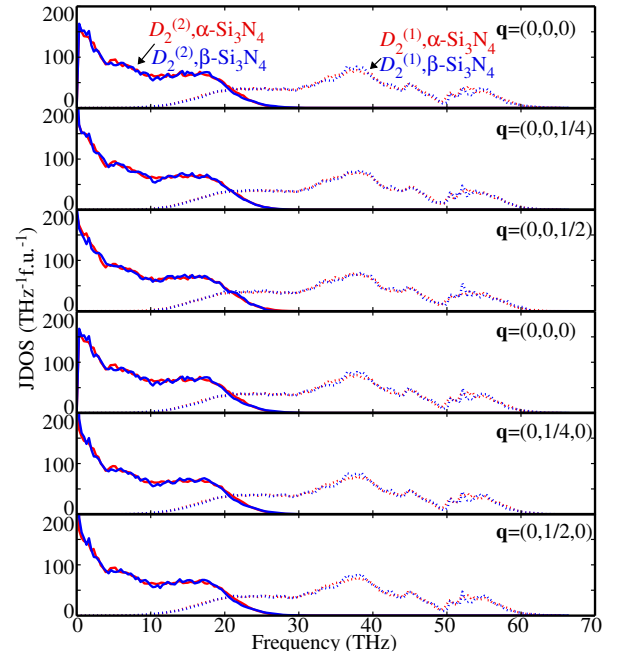


FIG. 6. (color online) JDOS of  $\alpha$ - and  $\gamma$ - $\text{Si}_3\text{N}_4$  at different  $\mathbf{q}$  points. The first and forth rows are JDOS at the same  $\Gamma$ -point but calculated with the polarization for non-analytic term correction set along  $c^*$  and  $b^*$ , respectively.

We hereafter focus on the comparison between the  $\alpha$  and  $\beta$  phases. As for the anisotropy in the  $\kappa$ , we find clear similarity between  $\frac{d\kappa_{ii}^c}{d\omega_\lambda}$  and WDOS with  $v_{\lambda,i}^2$ . The

remaining property, linewidth distributions are similar between the phases. The DOS are also similar. Therefore, the  $\mathbf{v}_\lambda$  simply account for the difference in the  $\kappa$  anisotropy between the two phases.

It is still curious that the linewidths are similar between these phases although their group velocities have marked differences. Thus we investigate this similarity further. Previously, Lindsay *et al.*<sup>40</sup> showed among many crystals of the zincblend structure a significant positive correlation between the  $\kappa$  and phase space available for the three-phonon scattering. The phase space was calculated by counting the number of three phonon configurations satisfying the selection rules for the energy and momentum conservation. The phase space is equivalent to the integration of the joint density of states (JDOS) over the frequencies and the Brillouin zone. More recently Togo *et al.* investigated the imaginary part of self-energy  $\Gamma_\lambda(\omega)$ . The  $\Gamma_\lambda(\omega)$  is related to  $\Gamma_\lambda$  by  $\Gamma_\lambda(\omega_\lambda) = \Gamma_\lambda$ . They showed that the frequency profile of  $\Gamma_\lambda(\omega)$  was characterized by JDOS.<sup>15</sup> Thus here we investigate the JDOS,  $D_2(\mathbf{q}, \omega)$ ,

$$D_2(\mathbf{q}, \omega) = D_2^{(1)}(\mathbf{q}, \omega) + D_2^{(2)}(\mathbf{q}, \omega) \quad (4)$$

where

$$\begin{aligned} D_2^{(1)} &= \frac{1}{N} \sum_{\lambda' \lambda''} \Delta(-\mathbf{q} + \mathbf{q}' + \mathbf{q}'') \\ &\times [\delta(\omega + \omega_{\lambda'} - \omega_{\lambda''}) + \delta(\omega - \omega_{\lambda'} + \omega_{\lambda''})], \\ D_2^{(2)} &= \frac{1}{N} \sum_{\lambda' \lambda''} \Delta(-\mathbf{q} + \mathbf{q}' + \mathbf{q}'') \\ &\times \delta(\omega - \omega_{\lambda'} - \omega_{\lambda''}), \end{aligned}$$

with  $\Delta(\mathbf{x})$  giving 1 if  $\mathbf{x}$  is a reciprocal lattice vector and otherwise zero. Fig. 6 shows the frequency-dependences of JDOS at different  $\mathbf{q}$ -points on the  $\Gamma$ -A and  $\Gamma$ -K paths, which show very slight  $\mathbf{q}$ -point dependence. Eq. (1) includes Bose-Einstein functions for the involved phonon modes and JDOS can be weighted with them as done in refs. 15 and 38, however we omit them for simplicity. With the weights, the absolute values are affected but the weighted JDOS of the  $\alpha$  and  $\beta$  phases are still similar. At the low frequency region responsible for the LTCs, among the two terms of  $D_2^{(1)}$  and  $D_2^{(2)}$  in Eq. (4), dominant is  $D_2^{(2)}$  which basically corresponds to the half part ( $\omega \geq 0$ ) of the auto-correlation function of DOS, which, for the  $\alpha$  and  $\beta$  phases, commonly show the frequency gap (Fig. 5-a).  $D_2^{(2)}$  curves reflect this DOS feature, dropping suddenly around 0 THz and showing a small shoulder around 5 THz, which corresponds to the width of the gap. Moreover  $D_2^{(2)}$  shows a broad peak around 18 THz, which corresponds to the frequency shift to make the largest correlation between the higher and lower portions of DOS across the gap. Because the gap is basically originated from the differences in the vibrations of the planer NSi<sub>3</sub> commonly contained in the  $\alpha$  and  $\beta$  phases<sup>39</sup>, the major shapes of  $D_2^{(2)}$ , reflecting this

gap feature, are similar in these phases. With the same origin, the JDOS of  $D_2^{(1)}$  are also similar in these phases.

Moreover, as indicated in Table. III,  $\Phi_{-\lambda\lambda'\lambda''}$  have similar impacts on the linewidths. With these similar impacts of JDOS and  $\Phi_{-\lambda\lambda'\lambda''}$  on  $\Gamma_\lambda$ ,  $\Gamma_\lambda$  in Fig. 5-d are similar.

As a small but interesting difference in the linewidths between these phases,  $\Gamma_\lambda$  below 5 THz in Fig. 5-d are aligned on a smooth line in the  $\alpha$  phase, while those in the  $\beta$  phase are scattered roughly onto two different lines. This difference can be explained by the vibration directions shown in Fig. 7. In Fig. 7-a,  $\Gamma_\lambda$  are classified using colors according to the sums of the squares of the eigenvector components along  $\mathbf{q}$ ; the sum is 1 for perfectly longitudinal waves. However, these sums have no clear contrast to distinguish the two branches in the  $\beta$  phase. Fig. 7-b shows the same plot as Fig. 7-a, but with colors according to the sums of the squares of the eigenvector components along the  $a$ - $b$  plane, which has 1 when the eigenvectors lie on the  $a$ - $b$  plane. There is a tendency in the  $\beta$  phase that  $\Gamma_\lambda$  are large for the vibrations along the  $a$ - $b$  plane. Therefore, within the single-mode RTA, for the phonon modes below 5 THz, all of which belong to the acoustic phonon branches, the vibration modes along the  $a$ - $b$  plane are more easily scattered in the  $\beta$  phase, no matter whether they are longitudinal or transverse. For the panel of  $\beta$ -Si<sub>3</sub>N<sub>4</sub> in Fig. 7-b, a straight line can divide the phonon modes into the two groups. The numbers of the phonon modes in the upper and lower parts are 157 and 58, whose ratio is rational as the population ratio of the vibration modes along and out of the  $a$ - $b$  plane.

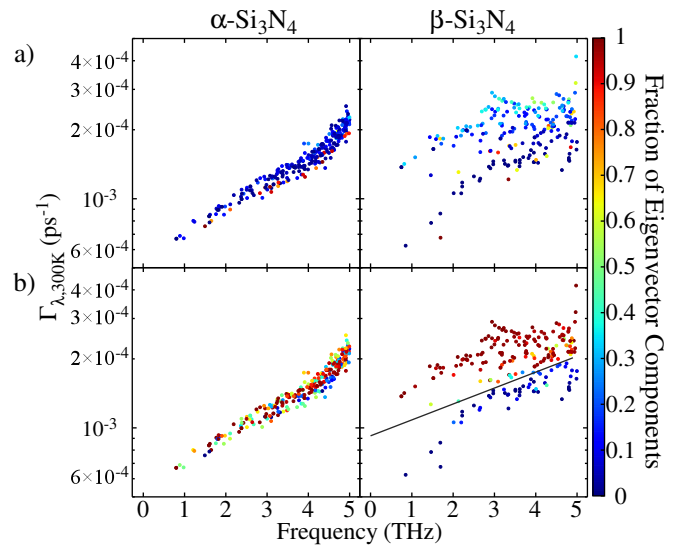


FIG. 7. (color online) Distribution of linewidths  $\omega_\lambda \leq 5$  THz with colormaps with respect to strengths of eigenvector components along  $\mathbf{q}$  (a) and on  $a$ - $b$  plane (b).

#### IV. SUMMARY

In the present study, we investigate the lattice thermal conductivities of the three  $\text{Si}_3\text{N}_4$  phases, by using the lattice dynamics based on the *ab-initio* interatomic force constants. The main remarks are as follows:

- 1) In the  $\alpha$ - and  $\beta$ - $\text{Si}_3\text{N}_4$ , whose crystal structures are characterized by the stacking manners of the basal layers, which alter the LTCs. In  $\alpha$ - $\text{Si}_3\text{N}_4$ , the LTC tensors are rather isotropic, while  $\kappa_{zz}$  of the  $\beta$  phase is much larger than the others, showing remarkable anisotropy in the LTC tensor.
- 2) In the  $\alpha$  phase, the acoustic mode phonons below 6 THz are the main heat carriers, while in the  $\beta$  phase, the phonons below 12 THz contribute to the thermal conductivity. Their group velocities are significantly different between the phases; their linewidths are basically similar due to the similar impacts of the phonon-phonon interaction strengths and selection rules. Therefore the differ-

ence in the group velocities alone qualitatively explains the difference of anisotropy.

**3) In the  $\gamma$  phase, the frequency distribution of the phonon mode contributions to LTC is found to be similar to that for  $\kappa_{xx}$  of  $\beta$ - $\text{Si}_3\text{N}_4$  although the respective phonon properties (group velocities and linewidths) are much different from those of the other phases**

#### ACKNOWLEDGMENTS

The present work was partly supported by Grants-in-Aid for Scientific Research of MEXT, Japan (Grant No. 15K14108 and ESISM (Elements Strategy Initiative for Structural Materials) of Kyoto University).

#### Appendix A: Pressure dependence of LTC of $\gamma$ -phase

\* k-tatsumi@imass.nagoya-u.ac.jp

- <sup>1</sup> G. Slack, Journal of Physics and Chemistry of Solids **34**, 321 (1973).
- <sup>2</sup> Y. Zhou, H. Hyuga, D. Kusano, Y.-i. Yoshizawa, and K. Hirao, Advanced Materials **23**, 4563 (2011).
- <sup>3</sup> K. Hirao, K. Watari, H. Hayashi, and M. Kitayama, MRS Bulletin **26**, 451 (2001).
- <sup>4</sup> K. Watari, Journal of the Ceramic Society of Japan **109**, S7 (2001).
- <sup>5</sup> N. Hirosaki, Y. Okamoto, M. Ando, F. Munakata, and Y. Akimune, Journal of the Ceramic Society of Japan **104**, 49 (1996).
- <sup>6</sup> F. L. Riley, Journal of the American Ceramic Society **83**, 245 (2000).
- <sup>7</sup> M. Yashima, Y. Ando, and Y. Tabira, The Journal of Physical Chemistry B **111**, 3609 (2007).
- <sup>8</sup> D. Du Boulay, N. Ishizawa, T. Atake, V. Streltsov, K. Furuya, and F. Munakata, Acta Crystallographica Section B: Structural Science **60**, 388 (2004).
- <sup>9</sup> S. Hampshire, H. Park, D. Thompson, and K. Jack, Nature **274**, 880 (1978).
- <sup>10</sup> T. Hahn, ed., International tables for crystallography, Vol. A (John Wiley & Sons, Inc., 2011).
- <sup>11</sup> T. Hirai, S. Hayashi, and K. Niihara, AM. CERAM. SOC. BULL. Am. Ceram. Soc. Bull. **57**, 1126 (1978).
- <sup>12</sup> N. Hirosaki, S. Ogata, C. Kocer, H. Kitagawa, and Y. Nakamura, Physical Review B **65**, 134110 (2002).
- <sup>13</sup> B. Li, L. Pottier, J. Roger, D. Fournier, K. Watari, and K. Hirao, Journal of the european ceramic society **19**, 1631 (1999).
- <sup>14</sup> R. Vashishta, R. K. Kalia, A. Nakano, and I. Ebbssö, Amorphous Insulators and Semiconductor, edited by M. F. Thorpe and M. I. Mitkova (Kluwer, 1996).
- <sup>15</sup> A. Togo, L. Chaput, and I. Tanaka, Physical Review B **91**, 094306 (2015).
- <sup>16</sup> A. Zerr, G. Miehe, G. Serghiou, M. Schwarz, E. Kroke, R. Riedel, H. Fueß, P. Kroll, and R. Boehler, Nature **400**, 340 (1999).

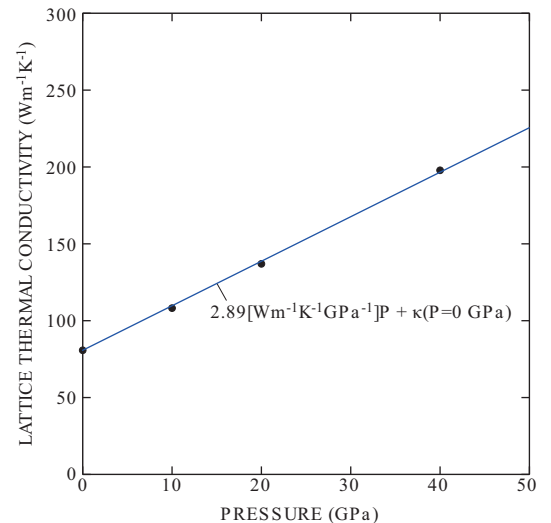


FIG. 8. (color online) Pressure dependence of LTC of  $\gamma$ - $\text{Si}_3\text{N}_4$ .

- <sup>17</sup> Y. Zhang, A. Navrotsky, and T. Sekine, Journal of materials research **21**, 41 (2006).
- <sup>18</sup> B. Xu, J. Dong, P. F. McMillan, O. Shebanova, and A. Salamat, Physical Review B **84**, 014113 (2011).
- <sup>19</sup> D. Morelli and J. Heremans, Applied physics letters **81**, 5126 (2002).
- <sup>20</sup> L. Chaput, Physical review letters **110**, 265506 (2013).
- <sup>21</sup> S.-i. Tamura, Physical Review B **27**, 858 (1983).
- <sup>22</sup> A. Togo and I. Tanaka, Scripta Materialia **108**, 1 (2015).
- <sup>23</sup> P. E. Blöchl, Phys. Rev. B **50**, 17953 (1994).
- <sup>24</sup> G. Kresse and J. Furthmüller, Physical review B **54**, 11169 (1996).
- <sup>25</sup> G. Kresse, J. Non-Cryst. Solids **193**, 222 (1995).
- <sup>26</sup> D. J. Kresse, Georg, Phys. Rev. B **59**, 1758 (1999).

- <sup>27</sup> J. P. Perdew, K. Burke, and M. Ernzerhof, Phys. Rev. Lett. **77**, 3865 (1996).
- <sup>28</sup> W. Paszkowicz, R. Minikayev, P. Piszcza, M. Knapp, C. Bähtz, J. Recio, M. Marques, P. Mori-Sánchez, L. Gerward, and J. Jiang, Phys. Rev. B **69**, 052103 (2004).
- <sup>29</sup> D. M. Ceperley and B. Alder, Physical Review Letters **45**, 566 (1980).
- <sup>30</sup> S. Wei and M. Chou, Physical review letters **69**, 2799 (1992).
- <sup>31</sup> Y. Wang, J. Wang, W. Wang, Z. Mei, S. Shang, L. Chen, and Z. Liu, J. Phys.: Condens. Matter **22**, 202201 (2010).
- <sup>32</sup> M. T. Dove, *Introduction to lattice dynamics*, Vol. 4 (Cambridge university press, 1993) pp. 76–77.
- <sup>33</sup> A. Ward and D. Broido, Physical Review B **81**, 085205 (2010).
- <sup>34</sup> R. Minikayev, W. Paszkowicz, P. Piszcza, M. Knapp, and C. Bähtz, “Thermal expansion of and silicon nitride,” (2007).
- <sup>35</sup> P. Andersson, Journal of Physics C: Solid State Physics **18**, 3943 (1985).
- <sup>36</sup> A. Cepellotti and N. Marzari, Physical Review X **6**, 041013 (2016).
- <sup>37</sup> R. J. Hardy, Physical Review B **2**, 1193 (1970).
- <sup>38</sup> S. Mukhopadhyay, L. Lindsay, and D. J. Singh, Scientific reports **6** (2016).
- <sup>39</sup> A. Kuwabara, K. Matsunaga, and I. Tanaka, Physical Review B **78**, 064104 (2008).
- <sup>40</sup> L. Lindsay and D. A. Broido, J. Phys.: Condens. Matter **20**, 165209 (2008).